

DOI: 10.1002/zaac.202100347



SnBrP-A SnIP-type representative in the Sn–Br–P system

Felix Reiter,^[a] Markus Pielmeier,^[a] Anna Vogel,^[a] Christian Jandl,^[a] Milivoj Plodinec,^[b] Christian Rohner,^[b] Thomas Lunkenbein,^[b] Katharina Nisi,^[c] Alexander Holleitner,^[c] and Tom Nilges*^[a]*Dedicated to Prof. Dr. Caroline Röhr on the Occasion of her 60th Birthday*

One-dimensional semiconductors are interesting materials due to their unique structural features and anisotropy, which grant them intriguing optical, dielectric and mechanical properties. In this work, we report on SnBrP, a lighter homologue of the first inorganic double helix compound SnIP. This class of compounds is characterized by intriguing mechanical and electronic properties, featuring a high flexibility without modulation of physical properties. Semiconducting SnBrP can be synthesized

from red phosphorus, tin and tin(II)bromide at elevated temperatures and crystallizes as red-orange, cleavable needles. Raman measurements pointed towards a double helical building unit in SnBrP, showing similarities to the SnIP structure. After taking PL measurements, HR-TEM, and quantum chemical calculations into account, we were able to propose a sense full structure model for SnBrP.

Introduction

One-dimensional systems are characterized by highly anisotropic optical, dielectric, conducting and mechanical properties.^[1] They feature, for example, an isolator type behavior perpendicular to the molecular or atomic chains of the material, but a semiconducting or conducting behavior along these chains.^[2] One-dimensional metallic systems however tend to be intrinsically unstable due to high fluctuation, nevertheless quasi-one-dimensional metals have already been synthesized.^[3] In the past few years, one dimensional semiconductors gained attention as promising candidates for electrochemical applications, mainly caused by their structural advantages compared with bulk counterparts. Their large specific surface area leads to

an improved light absorption by enhancement of the carrier collection.^[4] Another feature is the fast separation and collection of photogenerated charges, as observed in one-dimensional radial p-n junctions.^[5,6,7]

Fields of interest for one-dimensional compounds are photocatalytic water splitting applications and photovoltaics. Due to their unique electronic properties, significant improvements concerning the hydrogen evolution rate could be observed.^[8,9,10] ZnO/CdS nano-rod arrays have shown improved conversion efficiencies in the near infrared area compared to its planar counterpart in solar cells.^[11] One-dimensional nano-structured compounds are frequently applied as gas sensors. As they possess very high surface to volume ratios, they can adsorb more gas molecules and thus increase their receptor function and therein the sensitivity.^[12,13]

One promising one-dimensional candidate for energy conversion applications is the inorganic compound SnIP, which was reported by Pfister et al. in 2016.^[14] SnIP represents the first inorganic one-dimensional compound with an atomic scale double helical structure. An inner negatively charged phosphorus helix is surrounded by a positively charged tin-iodine helix. The resulting double helix exists in two enantiomeric forms. In the crystal structure of SnIP both a right-handed [*P*] and a left-handed [*M*] double helix occur, alternating along the *b*-axis, thus forming a racemic mixture. SnIP shows interesting electrical properties, a measured direct band gap of 1.86 eV (indirect band gap of 1.8 eV) and anisotropic mechanical properties along vs. perpendicular to the double helix axis. SnIP is characterized by a very low bulk modulus and a Young modulus as high as steel upon bending perpendicular to the double helix axis.^[15] As a consequence, SnIP needles can be reversibly bend up to 90° without any visible deterioration.

DFT calculations predict that SnIP, and its homologues may show very promising electronic properties for photocatalytic water splitting applications. DFT calculations on 32 different MXPn compounds (M=Si, Ge, Sn, Pb; X=F, Cl, Br, I; Pn=P, As)

[a] F. Reiter, M. Pielmeier, A. Vogel, C. Jandl, T. Nilges
Technical University of Munich,
Department of Chemistry, Lichtenbergstraße 4,
85747 Garching b, München, Germany
E-mail: tom.nilges@tum.de

[b] M. Plodinec, C. Rohner, T. Lunkenbein
Fritz-Haber-Institut der Max-Planck-Gesellschaft, Department of
Inorganic Chemistry,
Faradayweg 4–6, 14195
Berlin, Germany

[c] K. Nisi, A. Holleitner
Walter Schottky and Physics Department,
Technical University of Munich,
Am Coulombwall 4a,
85748 Garching, Germany

Supporting information for this article is available on the WWW under <https://doi.org/10.1002/zaac.202100347>

© 2022 The Authors. Zeitschrift für anorganische und allgemeine Chemie published by Wiley-VCH GmbH. This is an open access article under the terms of the Creative Commons Attribution Non-Commercial NoDerivs License, which permits use and distribution in any medium, provided the original work is properly cited, the use is non-commercial and no modifications or adaptations are made.

illustrate, that 17 of them should possess the double helical SnIP structure.^[17] Calculated band gaps of SnIP-type compounds may vary between 1.2–1.8 eV (PBE functionals), while HSE06 calculations resulted in band gaps of 2.21–2.96 eV.^[18] Band edge positions meet the fundamental requirement for the oxidation and reduction in water splitting reaction. Combined with their extremely high surface-volume ratio, that 1D rods possess, SnIP-type compounds may show benefits for water splitting applications in the future. Due to the reactivity of such materials in water the formation of core shell heterostructures are needed to allow such processes. Heterostructures of SnIP with inorganic hosts have already been tested for their water splitting ability. Promising results were reported for SnIP@C₄N₃(F,Cl) and SnIP@TiO₂ with significantly increased photocurrent density compared to the pure compounds.^[15,16]

We therefore wanted to synthesize more representatives of this class of materials. Most promising MXPn candidates (M=Si, Ge, Sn, Pb; X=F, Cl, Br, I; Pn=P, As) supposed to be PbIP, GeIP and SnBrP, due to only marginal structural differences compared with SnIP.^[18] A general trend was derived from the DFT calculations: the smaller the halide is, the closer the double helical rods move towards each other, until they form strong attractive interactions. If this happens a 2 or 3-dimensional network instead of double helices result. Also, most of the arsenic compounds showed inter-helical bonds, destroying the 1-D properties. We have therefore investigated the Sn–Br–P system (Figure 1) in order to realize the first SnIP homologue. Interestingly, the Sn–Br–P phase diagram is almost empty, only numerous binary phases exist. The only known ternary compound is the reported clathrate-type phase Sn₁₂P_{9,8}Br₄.^[19]

Results and Discussion

SnBrP was successfully prepared by a slightly modified mineralizer principle (short way transport reaction) approach following the SnIP protocol.^[20] We modified the SnIP synthesis in such a way, that the temperature was significantly lowered from 400 °C to 300 °C. Higher temperatures only yielded unwanted tin phosphides, mostly Sn₄P₃, and the clathrate phase Sn₂₄P_{19,6}Br₈. After cooling ampoules to room temperature, red-orange needles formed on the ampoule walls. Growth took place in a temperature gradient of 50 °C in star-like clusters featuring a crystal length of up to 200 μm. The basic transport mechanism seems to be quite similar to SnIP, which also forms clusters of needles via the gas phase and within a certain temperature gradient, however the crystal length and diameter of SnBrP are approximately 10 times smaller than for SnIP. For a determination of the atomic composition an EDS measurement was conducted on three different spots per crystal (Figure 2 b) featuring composition with a ratio of 1:1:1. Therefore, we can assume that the sum formula is very close to an atomic 1:1:1 ratio (Sn:Br:P). SnBrP is bright orange-red compared with the

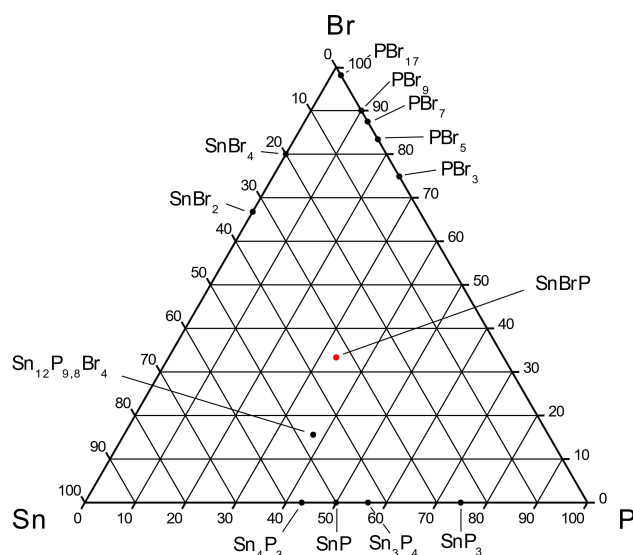


Figure 1. Ternary phase diagram of Sn–Br–P. The only known ternary compound is Sn₁₂P_{9,8}Br₄ so far.^[19]

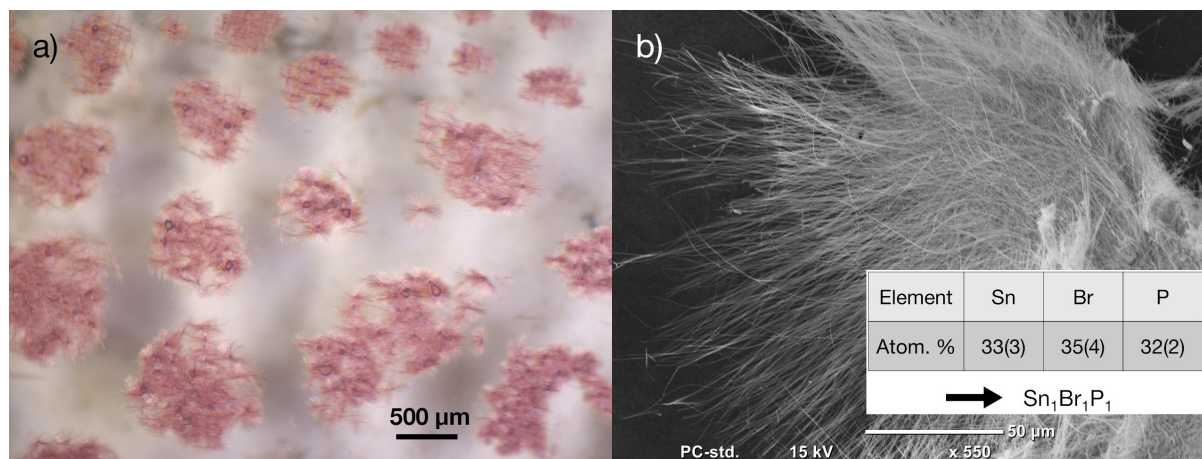


Figure 2. a) Images of red orange SnBrP needles on the ampoule glass wall taken with an optical microscope b) SEM image of SnBrP. Inset: Average atom percentage of a SnBrP sample with deviation according to EDS measurement of three different randomly chosen points.

dark red-brown color in case of SnIP. The color change is a first indicator of a slightly larger band gap in SnBrP (see later on). SnBrP crystals tend to cleave rapidly under mechanical stress along the needle axis which even can be observed upon touching or manipulating the bare crystals. This feature indicates weak van-der-Waals interactions between neighboring structure units (e.g. SnBrP rods, see Figure 3). We observed reduced crystallinity and severe stacking disorder for SnBrP (see later in the phase analysis section).

Raman Spectroscopy on SnBrP

Raman spectroscopy is a powerful tool to investigate structure units and the bonding situation in solids. We measured Raman spectra of SnBrP and SnIP and found a reasonably good accordance of band distribution and pattern in both cases. This feature may account for similar structure units in both compounds. (Figure 4 b). In order to verify this assumption, we calculated a Raman spectrum based on an optimized SnIP-type structure model for SnBrP by the aid of DFT (Figure 4 a).

Figure 4 shows a strong mode at 137 cm^{-1} , which can be attributed to the breathing mode of the outer [SnBr] helix. This is in good agreement with our calculations, according to which the mode should appear at 134 cm^{-1} . In this vibration, the Sn and Br atoms move directly towards the inner helix, whereby the helix diameter changes temporarily. The resulting breathing mode is depicted in Figure 5 a).

At 336 cm^{-1} and 350 cm^{-1} stretching vibrations of the inner phosphorus helix occur, where phosphorus atoms are trans-

lated along the helix axis. We calculated one of these modes (Figure 5 c) to occur at 329 cm^{-1} , which also matches our measurement very well. The breathing modes of the inner helix are localized at 450 cm^{-1} . This correlates with our calculation where a highly symmetrical breathing mode for the phosphorus helix (Figure 5 b) is predicted to be at 447 cm^{-1} . While the calculated modes for the stretching and bending modes regions of phosphorus qualitatively agree in position and intensity with the measured ones, the intensity varies for the [SnBr] part. Obviously, the SnIP model used for calculations does not perfectly reflect the accurate stacking sequence in SnBrP.

Taking a look onto the measured Raman spectra of SnIP and SnBrP it becomes obvious that the breathing mode of the outer tin-halide helix in SnIP is localized at 130 cm^{-1} , as opposed to the same mode at 137 cm^{-1} in SnBrP. A shift of this mode to slightly higher wavenumbers for SnBrP is reasonable, as bromine is lighter than iodine and bonds between lighter atoms tend to show modes at higher wavenumbers in a Raman experiment. The vibration of the inner phosphorus helix towards the outer SnI helix account for the mode at 217 cm^{-1} . This correlates well to the mode at 213 cm^{-1} in the SnBrP spectrum.

The stretching vibrations of the inner phosphorus helix in SnIP are represented by the modes at 338 cm^{-1} and 350 cm^{-1} . Similar ones are present in SnBrP at 336 cm^{-1} and 350 cm^{-1} . Due to the propagation of the mode along the phosphorus helix, the outer tin-halide helix does not affect the inner phosphorus helix and therefore mode positions are rather similar. A substitution of the halide does not shift the modes, as

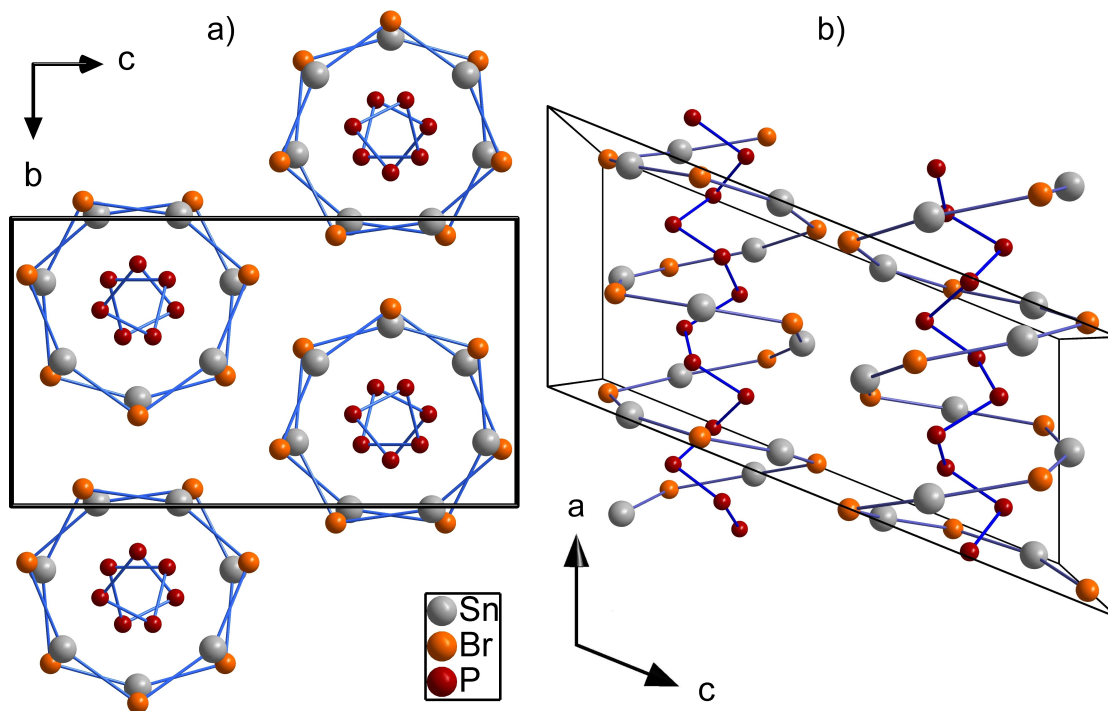


Figure 3. Proposed crystal structure model based on the SnIP structure. SnBrP structure model projected along the *a* (a) and *b* axis (b). [SnBr] and [P] helices are forming a double helical SnBrP rod.

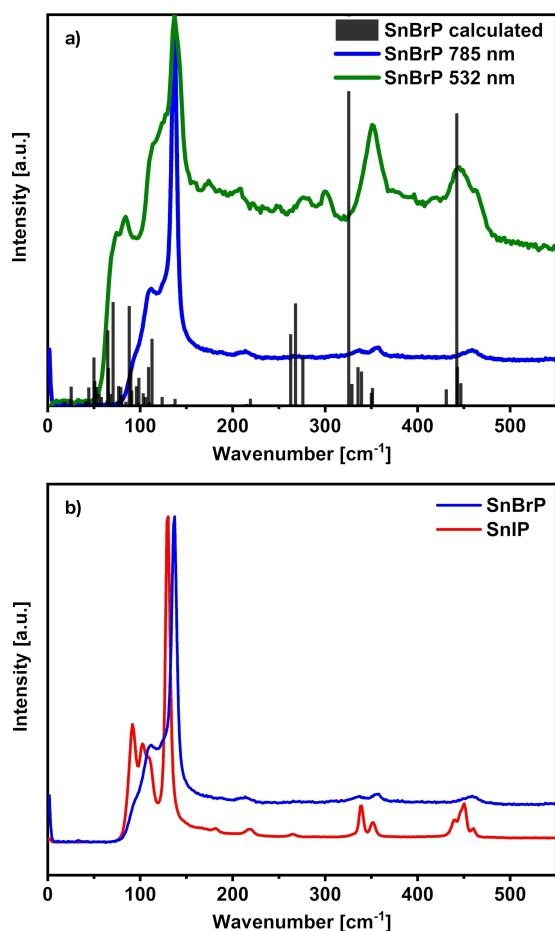


Figure 4. a) Recorded Raman spectra of SnBrP with a 532 nm laser (green line) and a 785 nm laser (blue line). Calculated Raman modes based on a SnIP-type structure model according to Figure 3 and derived from DFT data are drawn with black lines. b) Recorded Raman spectra of SnBrP (blue line) compared to SnIP (red line).

illustrated in our measurement. On the other hand, the breathing vibration of the phosphorus helix is perpendicular to the propagation direction of the double helix. Halide substitution from iodine to lighter bromine reduces the diameter of the outer helix and thus reduces the space in which the inner phosphorus helix can vibrate. This results in a higher force constant and thereby a blue-shift of mode in the Raman spectrum.

With a wavenumber of 450 cm^{-1} for SnIP and 458 cm^{-1} in the SnBrP Raman spectrum, this effect is confirmed by the measurement. In sum, the presence of comparable bonding properties in SnBrP and SnIP and therefore similar building blocks seems highly feasible. We therefore conclude that SnBrP contains similar double helical structure units as SnIP.

Photoluminescence measurements on SnBrP

DFT calculations predicted a slightly larger band gap for SnBrP than for SnIP. Figure 6 shows a measured photoluminescence

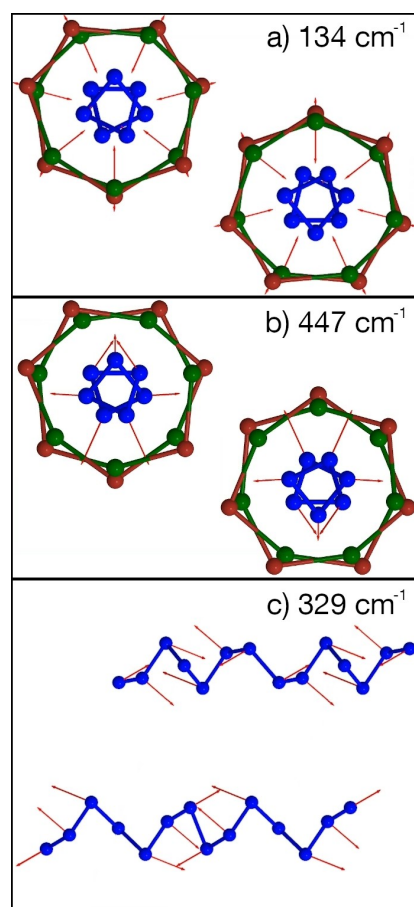


Figure 5. Illustration of three different vibrations of a SnBrP double helical rod including their calculated wavenumber. Red arrows indicate the direction of atom movement during the vibration. a) Breathing vibration of the outer Sn–Br helix. b) Breathing vibration of the inner P helix. c) Stretching vibration of the inner P helix. The Sn and Br atoms are not drawn for better visibility.

spectrum of SnBrP, where a broad anisotropic peak is visible at 1.93 eV. At least two peaks are present as shown by deconvolution in Figure 6. We fitted the measured data with Voigt curves and received a satisfying result with two broad peaks at 1.85 eV and at 1.96 eV. This matches its colour perfectly, since all light with wavelengths higher than 628 nm is absorbed by the compound and the only reflected visible light is in the red and orange region. Comparing these peaks of SnBrP to the PL spectrum of SnIP featuring two peaks at 1.8 eV and 1.86 eV, a slight blue shift for SnBrP becomes apparent. This is the same trend other main group semiconductors show. Lighter atoms within the same group possess a higher electronegativity, which increases the energy difference between valence and conduction band edges. Thus, substituting an atom with its lighter homologue in the same structure, tends to increase the band gap. In conclusion, SnBrP and SnIP seems to be composed of comparable double helix rods.

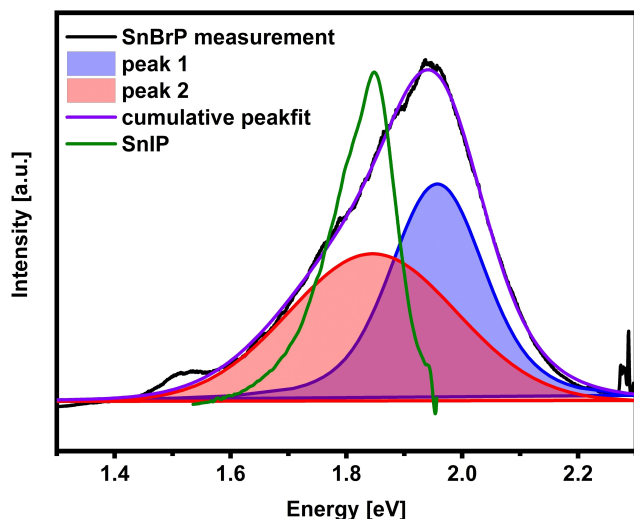


Figure 6. Photoluminescence spectrum of SnBrP. The measured intensity (black line) was fitted with two Voigt curves (red, blue) indicating two different band gaps. The cumulative fit (purple line) matches the measured data very well with a coefficient of determination of 0.997. The photoluminescence of SnIP is given as reference (green line).

Differential Scanning Calorimetry (DSC)

Thermal stability of SnBrP was measured with differential scanning calorimetry, as shown in Figure 7. Started with needle shaped crystals of 1:1:1 composition (Sn:Br:P atomic ratio) we identified no significant thermal effect during the first heating cycle up to 278 °C. At approximately 280 to 290 °C SnBrP starts to melt/decompose characterized by a weak endothermic effect which is directly overlaid by multiple exothermic effects at

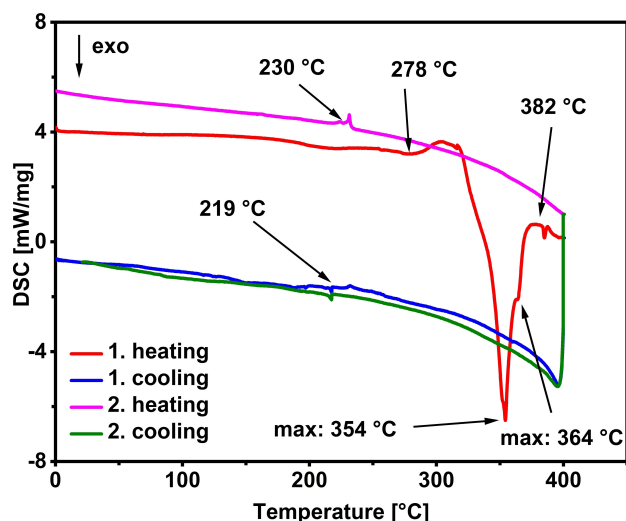


Figure 7. Differential scanning calorimetry heating and cooling curves of a SnBrP sample. Two cycles were recorded reaching from 0 °C to 400 °C. Arrows mark the onset temperatures for thermal effects unless otherwise stated.

higher temperatures. The first strong and defined exothermic peak occurs at 354 °C (maximum T) with a shoulder at lower temperatures (and another one at higher temperatures (364 °C, maximum T)). We assign these three exothermic effects to the formation of three crystalline phases. At 384 °C (maximum T) (382 °C, onset value) a fourth exothermic effect was found which represents another crystallization process. We expect in total four different solids during the thermal decomposition of SnBrP. We stopped heating at 400 °C and cooled down to –150 °C (not fully shown in Figure 7). During first cooling only one significant exothermic effect occurs at 219 °C (onset) which represents the crystallization of Sn. During another heating/cooling cycle we see a weak endothermic effect at 220 °C (m.p. SnBr₂ 216 °C) and the melting of Sn at 227 °C (m.p. Sn 232 °C). In sum, SnBrP decomposes slightly above 280 °C to multiple crystalline solids and liquid Sn. Due to the maximum temperature of 400 °C applied to the DSC sample we observed no melting or boiling points of the solid decomposition products. The needle shaped morphology of the starting material remained in the final product after thermal treatment.

To investigate the decomposition of SnBrP after the DSC experiment we opened the aluminum crucible and conducted an XRD measurement. SnP, Sn₄P₃ and Sn were detected as crystalline decomposition products (see Figure S3). This corresponds well with our DSC measurement, where we could observe tin after the decomposition and crystallization at room temperature. The melting points of Sn₄P₃ and SnP are above 400 °C (dec Sn₄P₃ 550 °C; SnP 540 °C) and were therefore not detected here. We also recorded an SEM image and conducted an EDS measurement. The morphology of the needles remained intact as clearly illustrated in Figure S4 after the DSC experiment. EDS measurement of the sample showed a composition of the residual needles of 1:1:2, resulting in a chemical formula of "SnBrP₂". Such a compound has not been reported in the literature so far to the best of our knowledge (cf. Figure 1). Therefore, beside the formation of a single compound, the 1:1:2 composition can be caused by averaging of many different solids during the semi-quantitative elemental analysis. Assuming the evaporation of "SnBr" from SnBrP during the first decomposition step at ~280 °C can directly lead to a compound with the composition SnBrP₂. The formation of SnBr₂ can be explained via hypothetical transformation of "SnBr" into Sn and SnBr₂. If all identified solid phases are taken into account one must assume another phosphorus rich species (like "SnBrP₂") or elemental phosphorus as an additional decomposition product. We found no hints for phosphorus formation in our experiments, therefore a formation of a new ternary Sn–Br–P phase cannot be fully ruled out.

SnBrP decomposes into SnP, Sn₄P₃, Sn, SnBr₂. Yet unknown ternary "SnBrP₂" or another phosphorus rich phase are possible further products during heat treatment. In sum, the thermal decomposition of SnBrP occurs at a relatively low temperature and due to its (rather complex) decomposition behavior it is not suitable for high-temperature applications.

XRD-measurements on SnBrP

Powder and single crystal XRD data were collected in order to determine the crystal structure of SnBrP. Data were collected in our lab as well as at the Diamond Light source synchrotron radiation facility, Didcot, UK, in order to achieve best possible data quality. Powder diffractograms only show reasonable quality if very long acquisition times are applied. A representative diffractogram with an acquisition time of 60 h (on a modern semiconductor detector) is given in Figure S1 (Supplement). It was not possible to derive a proper unit cell or structure model from these data. If 'single crystals' are collected for single crystal structure data acquisition the underlying problem becomes obvious. Defined periodicity is only found in two directions and the third one is fully non-periodic. We measured in the order of 50 or more crystals in our lab and 10 crystals at the Diamond facility. In each case, a proper translation periodicity was not found. As shown earlier on, either the pronounced cleavage tendency, beam sensitivity or a high moisture or air sensitivity may be the reason for this behaviour.

One possible explanation is somehow related to the cleavage tendency or caused by it. A different stacking of the double helical rods can occur if SnBrP double helices may shift parallel to each other by mechanical stress. As a result many different structure models may form. We illustrate this feature in Figure 8 where different double helix isomers are stacked in various ways. Figure 8 d shows the view along the *b* axis of SnBrP rods if they were arranged like in SnIP. In e) and f) two different arrangements are depicted, where we did not alter the middle rod, but adjacent rods are shifted along the *a* axis. This creates a different unit cell and different diffraction pattern, while still containing the same structural building units. Alternatively, instead of shifting the double helical rods against each other, they could also show partial dislocation. A third option is the occurrence of different amounts of [*M*] and [*P*]-helix enantiomers.^[21] SnIP consists of a racemic mixture of enantiomers as shown in Figure 8 a. However, it is also possible that different enantiomers are arranged shell-wise around a central rod (Figure 8 b), or that layers of different chiral rods alternate along the diagonal *b*-*c* direction (as shown in Figure 8 c). This is only an example of three possible arrangements, naturally an almost infinite number of models exist. A variable distribution of chiral double helices in SnBrP can also affect the crystal symmetry and therefore may result in different unit cells. Hence, it is possible to generate multiple theoretical XRD patterns for SnBrP, all consisting of the same double helical building unit, but having them arranged in different patterns of [*M*] and [*P*] helices. Of course, a necessary condition for X-ray structure solution is a three dimensional periodicity in all cases.

We also conducted numerous single crystal diffraction experiments as mentioned earlier. All XRD experiments in our lab pointed towards a very severe stacking order problem for all candidates. In each case we only found reflections which were originated from 2D ordering only. Such data are not sufficient for structure solution or refinement. In order to check if a higher intensity of X-rays and therefore much smaller

crystals might be a solution, we also measured SnBrP representatives with synchrotron radiation at the Diamond Light Source. Unfortunately, even such data did not allow a proper crystal structure determination. (see Figure S2) The question quickly arose if SnBrP might be air, moisture or beam sensitive and therefore quickly degenerates upon radiation. We handled SnBrP in inert gas atmosphere prior to our measurements to set air and moisture problems to a minimum. To validate the beam sensitivity and to gain more reliable structure data we conducted HR-TEM measurements.

HR-TEM on SnBrP

HR-TEM were conducted at the Fritz-Haber Institute in Berlin using state-of-the-art HR-TEM techniques and taking a possible beam sensitivity of the samples into account. The used samples were handled under argon atmosphere to avoid any surface oxidation. High-resolution TEM (Figure 9) indicates, that the surface and a few nanometres of SnBrP needles often show an amorphous character. The layer forms immediately under exposure to the high intensity beam necessary for HR-TEM and then slowly grows to a thickness of 5–10 nm within 3–4 minutes of exposure, after which the sample appears to become stable. Serial electron diffraction shows that the core structure of the needles remains unaffected during exposure (Figure S9).

All diffraction patterns show streaks of scattering intensity between the reflections perpendicular to the needle rotation axis, indicating a modulated structure (Figure 10). The patterns cannot be indexed to the proposed SnIP-type SnBrP-structure nor to the only known ternary structure $\text{Sn}_{12}\text{P}_9\text{Br}_4$ (space group *Pm3n* (No. 223),^[19]). Fourier filtered HRTEM of an edge region of the needle shown in Figure 10 a) in the same orientation as Figure 10 c) is presented in Figure 11. The image was filtered in such a way, that the streak intensity between spot maxima was removed while preserving the intensities from all spots visible in the FFT and those present in the ED patterns (Figure S10, Figure 10 b–c).

We observe a gradual change of the lattice contrast with increasing distance from the needle edge without distinct grain boundaries. The patterns resemble those emerging under rotation of a single crystal through multiple zone axes. As the Raman measurements strongly suggest that the double helix is the base structural motif, one can assume that the helix axes lie parallel to the needle axis. A phase contrast, that could stem from the helical structure, was observed in the HRTEM images (marked by the asterisk (*) in Figure 11 c), and supports this assumption (compare 010 projection in SnIP.^[14] The TEM observations thereby indicate that the packing of the helices is modulated rotationally around the needle axis but fully crystalline parallel to the needle axis. Crystalline structures which do not show strict translational order in 3D are described in the literature using the terms "rotating lattice single crystals (RLS)" or "transrotational crystals".^[23,24] The fact that only 2D information could be gathered in the single crystal XRD measurements can be explained by assuming that the present SnBrP structure falls under the class of such RLS crystals. As the

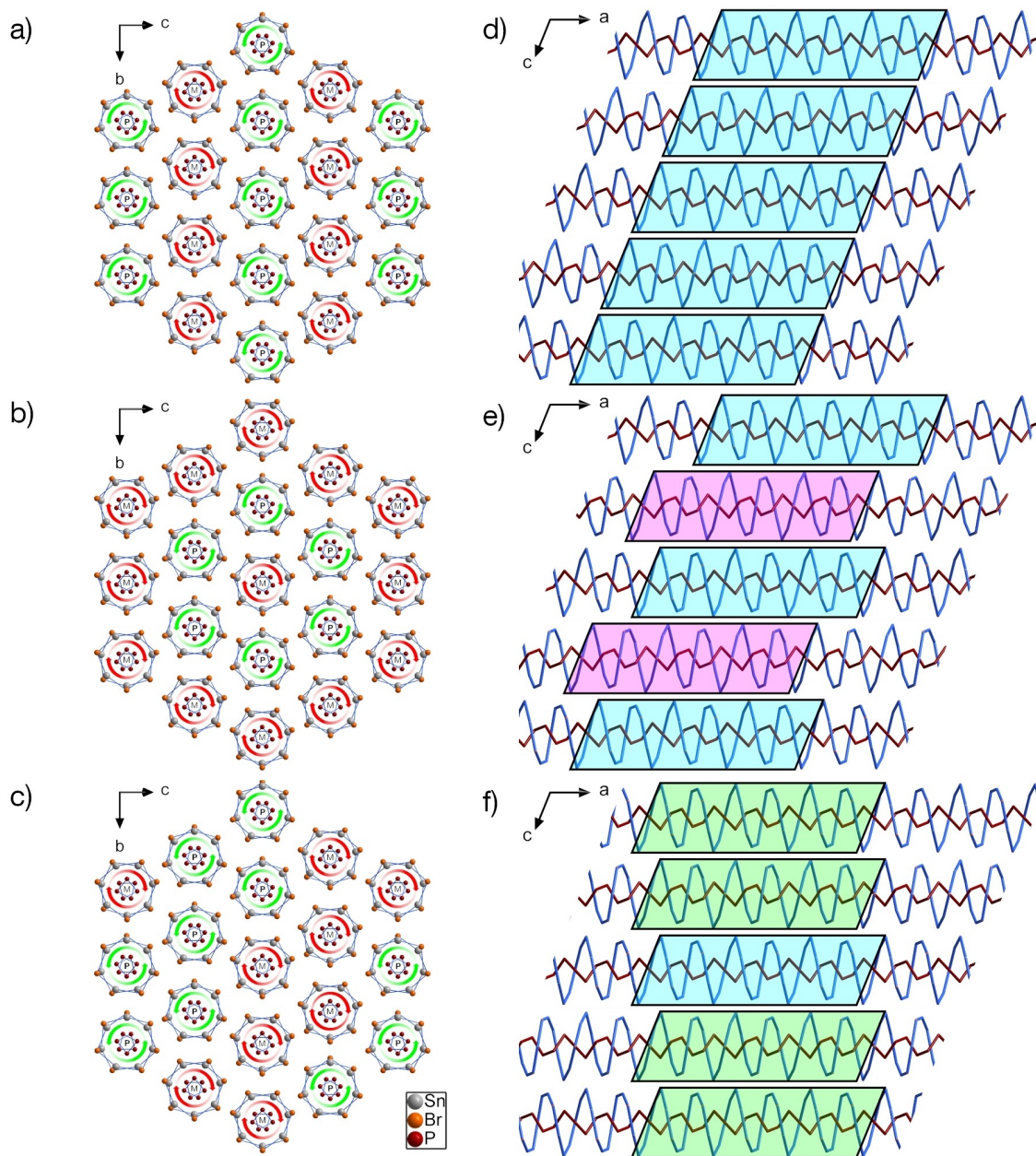


Figure 8. Selection of possible structure models for SnBrP constructed by parallel [M] or [P] double helices (a–c). The view along the *a* axis is shown in a–c, where different arrangements of the chiral [M] (red) and [P] (green) rods are depicted. In d–f the structure model is shown along the *b* axis. A block of three repeating units of the rods is highlighted, while blue signalizes that they have the same position as they would have according to our calculations. The rods with purple and green color are shifted along the *a* axis. The couple a/d represent the stacking of rods in SnIP. b/e, and c/f represent two examples of differently packed double helix rods.

building blocks of the needle exist locally in different orientations rotated around the axis parallel to the needle axis, a scattering experiment integrated over the whole needle diameter, simultaneously shows the diffraction from many crystallographic zone axes which are all perpendicular to the needle axis. In this case a rotation around the needle axis only gives a small change in the set of zone axes that contribute to the scattering intensity. This creates the impression that the needle has not rotated.

A deeper combined analysis of the powder XRD pattern and the HRTEM images might allow the determination of the unit cell, as the HRTEM image reveals the angles between planes of certain *d*-spacings. Plugging this information into the single crystal analysis could then give the local packing structure.

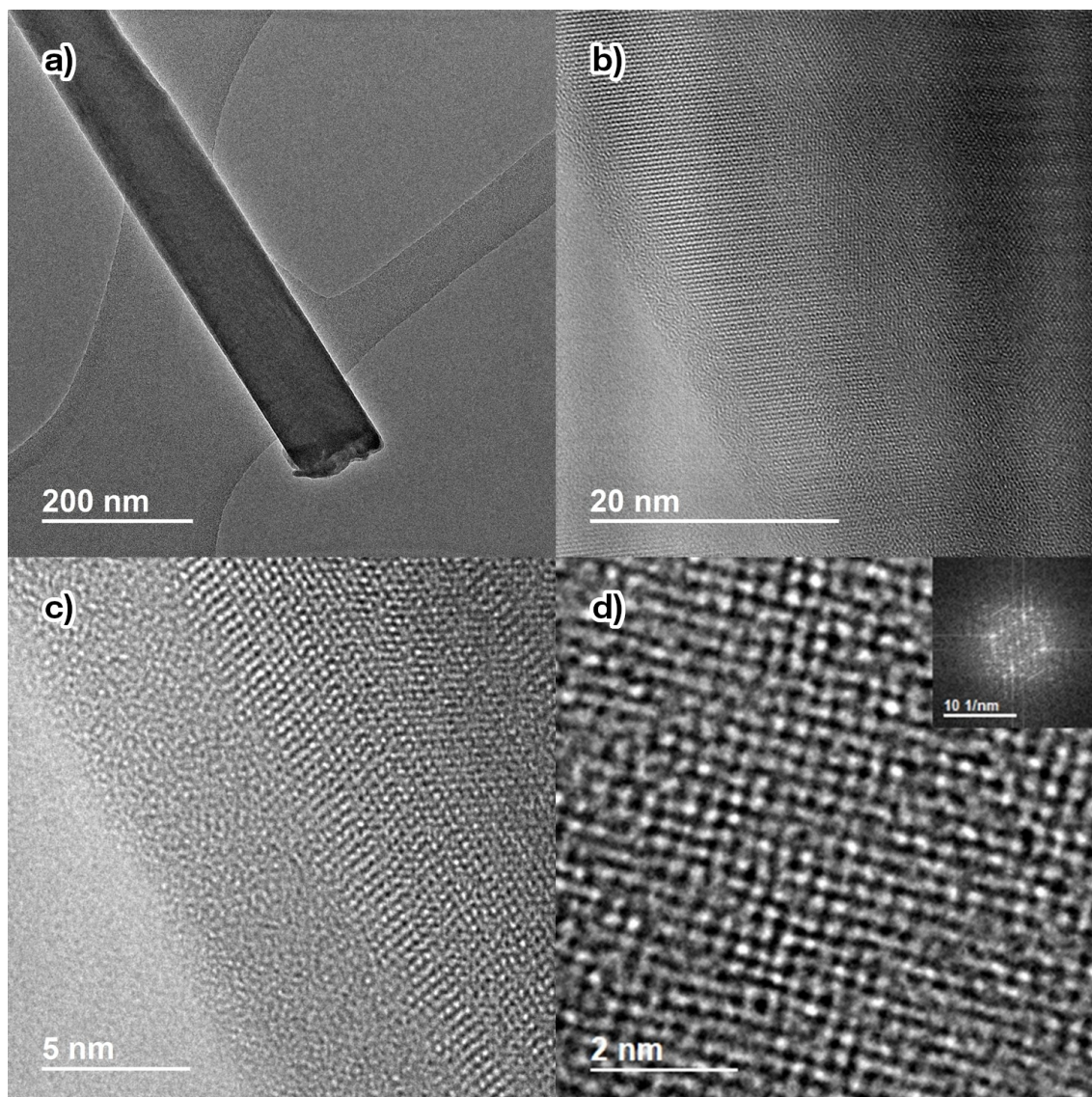


Figure 9. High-resolution transmission emission microscopy images of SnBrP needles with different magnifications. An amorphous region of 5 nm at the surface of SnBrP needles can be observed. d) shows a selected SnBrP area featuring strong disorder also illustrated in the SAED pattern in the inset.

XPS Measurement on SnBrP

As the HR-TEM images showed a thin amorphous layer with approximately 5 nm thickness on top of the SnBrP needles, we conducted XPS measurements to examine the surface species. SnBrP crystals were prepared and stored under protective gas atmosphere prior to the measurements. During the transport into the XPS chamber air contact of the SnBrP samples could not be avoided.

In the elemental scan shown in Figure S5 15 atom-% Sn, 5% Br, 7% P, 41% O and 31% C can be detected. The ratio of tin, bromine, and phosphorus reveals that the surface layer does not consist of SnBrP. With a high oxygen contribution it becomes apparent, that most of the surface species consists of oxidized compounds. The Sn 3d region in Figure 12 a) shows

only the expected doublet peaks without splitting or noticeable shoulders, but as there are no large shifts expected for Sn, this does not rule out the presence of more than one species. For the P 2p peaks shown in Figure 12 b) a clear splitting into oxidized (higher binding energy) and reduced (lower binding energy) P species can be observed. The presence of oxidized phosphorus proves the previously assumed hypothesis of surface oxidation of SnBrP. Thus, the amorphous layer seen in the TEM most likely contains oxidized phosphorus species like phosphates. But as this layer is only a few nanometers thin, the XPS does also detect the reduced phosphorus in the $^{1d}[P]_{\infty}$ helix of SnBrP.

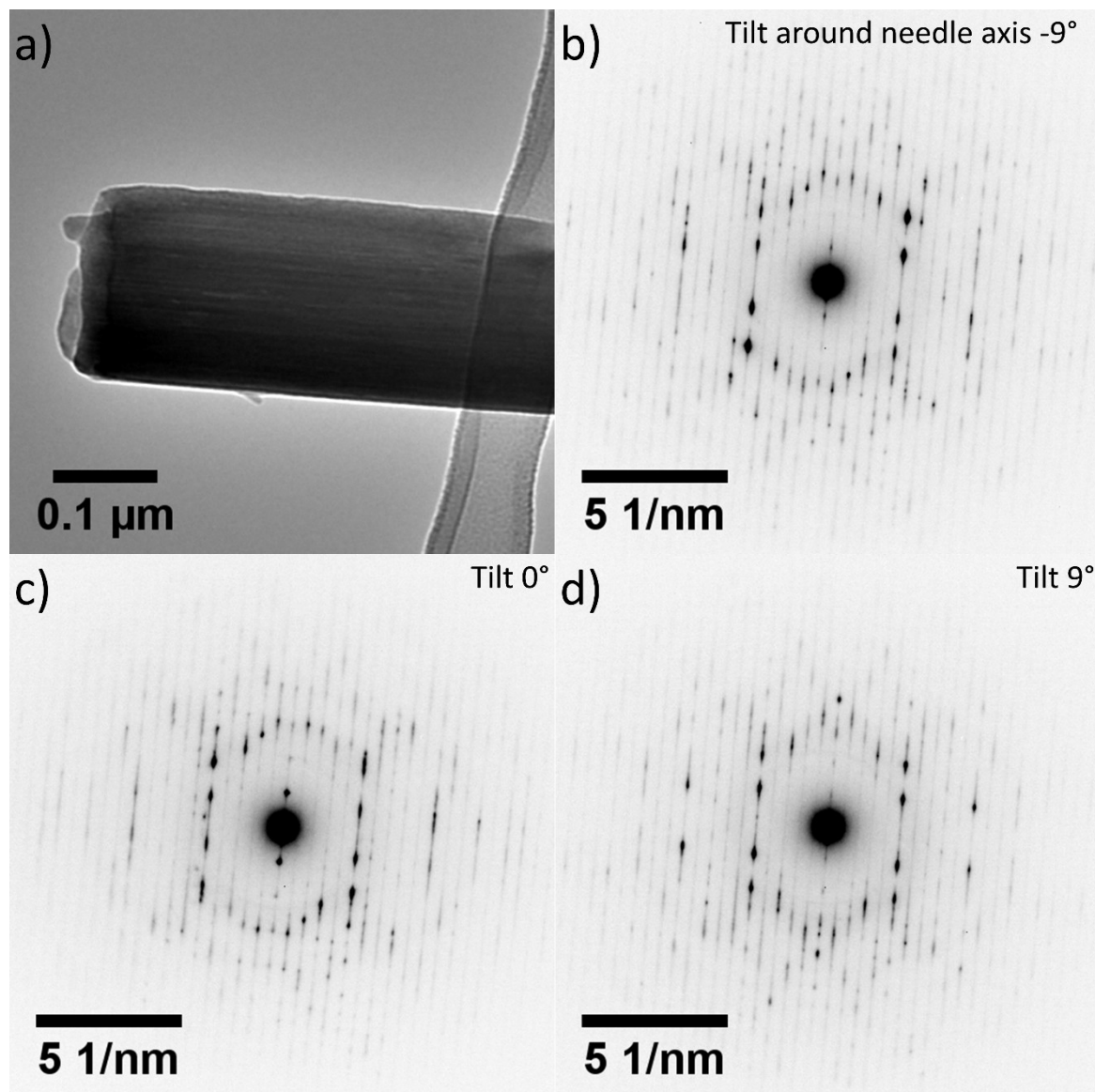


Figure 10. a) TEM of an SnBrP needle. b–d) ED measured on the needle with different sample tilt around the needle axis. The ED patterns all show an unusual, high amount of streak intensity between Laue spots. The streak intensity is lying exclusively on axes perpendicular to the needle axis. The patterns could not be indexed to individual zone axes.

Discussion Section

We synthesized a new compound in the ternary Sn–Br–P system with 1:1:1 composition and a band gap of 1.93 eV. SnBrP can be prepared reproducibly but in low yields. Optimization of the synthesis process to increase yield by altering parameters like the educts (P_{red} , P_{white} , SnBr_2 , SnBr_4 , PBr_3 , Br_2 ; in any combination), temperature, cooling rate or temperature gradient, as well as changing the ampoule length and starting material amount failed. The best results were achieved if the synthesis temperature was set close to $T_{\text{decomposition}}$ but the formation window is rather small. At temperatures of more than 20 K away from $T_{\text{decomposition}}$ a product formation was not observed anymore.

Raman spectroscopic investigations on SnBrP proved that the title compound consists of similar double helical building units as compared with SnIP. These building units can however be stacked in various ways, resulting in different crystal structures for SnIP and SnBrP. The tendency of SnBrP to form a 3D periodic structure is very low, most likely due to severe stacking disorder. HR-TEM measurements suggest a sensitivity of SnBrP against hard radiation which caused surface amorphization of SnBrP crystal during the measurements. Nevertheless, we were able to illustrate, that SnBrP shows a certain order in two, but not in three dimensions. SnBrP obviously belongs to the class of RLS materials where parts of the structure are rotated relative to each other on very short length scales. We believe that SnBrP double helices bundles are stacked differ-

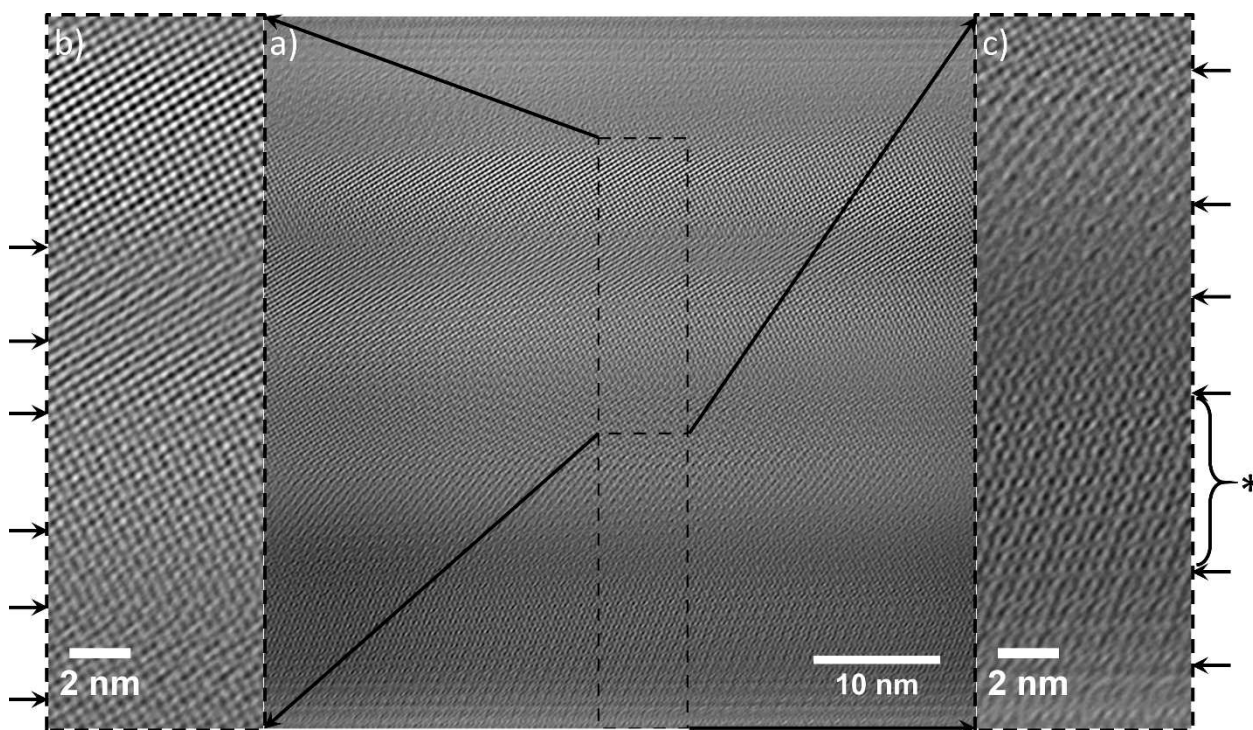


Figure 11. a) Fourier filtered HRTEM of an SnBrP needle. b,c) magnified view of the sections in a) as indicated by the dashed boxes. The original image and the fourier mask are given in the supporting information (Figure S10). The arrows on the sides indicate the approximate transitions between zone axes caused by the rotation of the crystal lattice. The region marked by the asterisk (*) shows very similar contrast to the view along the 010 zone axis in the SnIP structure, where the helices are viewed side-on and are stacked along the viewing direction.

ently on a 4 nm length scale which renders a structure determination problematic.

XPS measurements showed, that the surface of SnBrP is often partially oxidized, thus handling under protective gas atmosphere is needed. Even for crystals handled on air for only a few minutes, oxidation cannot be fully avoided. Such a sensitivity has to be taken into account if SnBrP may transferred into applications.

Obviously, the synthesis of SnBrP via short way vapor transport needs to be optimized or replaced by other techniques, prior to any usage of SnBrP in applications. A more promising way might be a solvothermal synthesis at lower temperatures to avoid formation of thermodynamically more stable by-products like Sn_4P_3 or SnBr_2 . Also the strong decomposition tendency at high temperatures might be overcome by this process.

Conclusion

SnBrP represents a new compound in the ternary Sn–Br–P system. It is accessible via short way transport reaction as thin red-orange needles, which are very flexible and tend to cleave easily. Semi-quantitative elemental analysis substantiated the 1:1:1 composition which defines SnBrP as the second ternary compound in the Sn–Br–P system. In a combined set of experiments, including Raman spectroscopy, PL measurements,

HR-TEM and quantum chemical calculations a sense full structure model was postulated, substantiating a double helix substructure in SnBrP. Especially the significant equivalency of calculated and measured vibration modes of SnBrP strengthens the assumption of a double helical structure in SnBrP. However, a structure determination via single crystal diffraction did not yield a promising result, due to the lack of 3D periodicity. According to HR-TEM investigations SnBrP belongs to the class of rotating lattice single crystals (RLS). Very weak bond interactions between the double helices cause this feature which accounts for severe stacking disorder. A bandgap of 1.93 eV was observed by photoluminescence spectroscopy for SnBrP which is slightly larger than the band gap of SnIP and in accordance to calculated values.

Experimental Section

Synthesis of SnBrP: A mixture of Sn (38.8 mg, 99.999% CHEMPUR) and red phosphorus (20,2 mg, 99.999 + %, CHEMPUR) were weighed in a silica glass ampoule (\varnothing 10 mm, 1 mm wall thickness). After adding SnBr_2 (91,0 mg, 99,2%, ALFA AESAR) in a glovebox (MBraun UniLab, $\text{O}_2 < 0,1$ ppm, $\text{H}_2\text{O} < 0,1$ ppm), the ampoule was evacuated ($p < 10^{-3}$ mbar), sealed with a hydrogen burner and placed in a NABERTHERM muffle furnace (L3/11/330) with the educts at the hot zone. It was heated up to 300 °C within 3 h, kept at this temperature for 2 days and then cooled down to room temperature with 2.5 °C/h. Attention, due to the natural temperature gradient in the oven we reach a temperature below the decomposition temper-

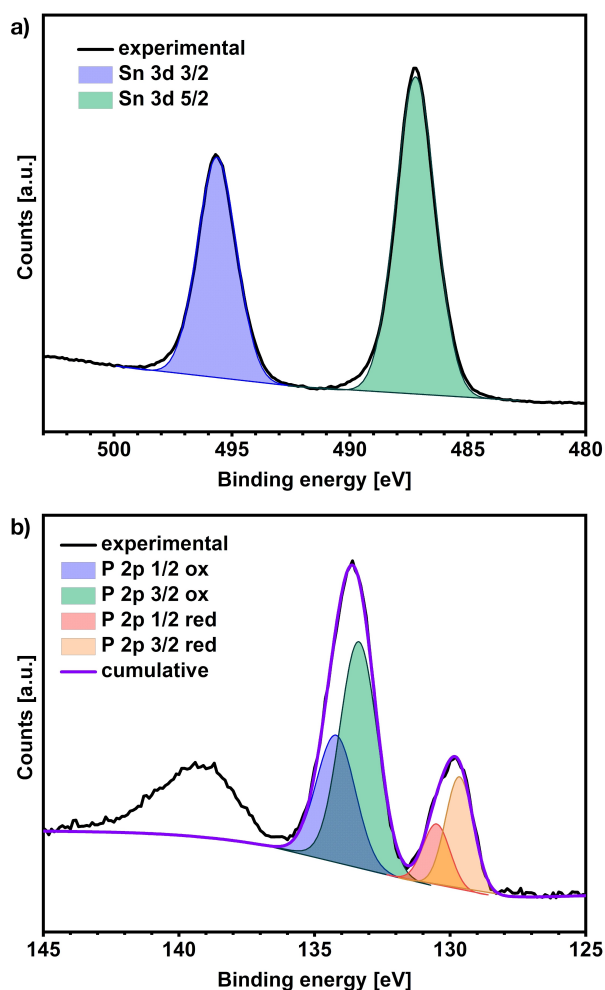


Figure 12. XPS spectra of SnBrP a) Sn 3d region b) P 2p region. The broad peak at 140 eV is caused by the Sn 4s electrons.

ature of 280 °C within the ampule. The product crystallized as orange needles on the ampoule wall along the temperature gradient with an estimated yield < 1 mass-%.

XRD-Measurement: X-ray powder data were collected on a Stoe Stadi P diffractometer (Cu-K α_1 radiation, $\lambda = 1.54051$ Å, Ge-monochromator) using a DECTRIS Mythen 1K detector. An external calibration was performed using Si ($a = 5.43088$ Å). Phase analysis and indexing was performed with the program package Stoe WinXPOW.

Single crystal XRD: Single crystal XRD measurements were performed with synchrotron radiation ($\lambda = 0.68890$ Å) at Diamond Light Source, Didcot, UK, at beamline I19. The diffractometer, manufactured by Crystal Logic, was equipped with a Rigaku Saturn 724+ CCD detector and an Oxford Cryostream Plus system. Data reduction was performed with the Rigaku CrysAlis Pro Software. Single crystal data was also collected with a Stoe IPDS II diffractometer with Mo-K α_1 radiation, a graphite monochromator and an image plate detector system. The data was processed using the X-Area software suite.

Scanning Electron Microscopy (SEM) and Energy Dispersive X-ray Spectroscopy (EDX): The samples were fixed on a graphite holder with a conductive adhesive polymer tape from PLANO GmbH. The SEM images and EDS analysis were performed using a JOEL JCM-

6000 NeoScop™ with an integrated JOEL JED-2200 EDS unit. The acceleration voltage was set to 15 kV. The EDS results were averaged from at least three different point, selected randomly on the crystal surface.

Differential Scanning Calorimetry (DSC): Thermal analysis was conducted on a NETZSCH DSC 200 F3 Maja calorimeter. About 2 mg of sample were sealed in an aluminium crucible in an argon filled glovebox. An empty sealed crucible served as a reference. The measurement was performed under a nitrogen flow of 100 mL/min while heating up to 673 K with a rate of 10 K/min. The DSC data was processed using the PROTEUS Thermal Analysis software.

Raman Spectroscopy: Raman spectra were recorded at 300 K using a Renishaw inVia RE04 Raman microscope equipped with a Nd:YAG laser ($\lambda = 785$ nm) and a CCD detector. A low laser power of 0.1 mW was applied to avoid decomposition of the sample and a total number of 300 scans were recorded.

Photoluminescence Spectroscopy: A WITec alpha300R (WITec GmbH, Ulm) equipped with a Olympus LMPlanFL N 50x/0.5 objective was used to acquire the photoluminescence (PL) spectra. The sample was sealed in a quartz capillary under argon atmosphere and irradiated with a 532 nm laser with 0.15 mW and a 300 g/mm grating. Each measurement was integrated for 30 seconds with 3 accumulations.

XPS Measurement: X-ray photoelectron spectroscopy (XPS) spectra were acquired with a Kratos Axis Supra spectrometer using monochromatic Al K α radiation ($h\nu = 1486.6$ eV) with a total power of 225 W under ultra-high vacuum ($< 10^{-8}$ Torr). The emission current was 15 mA and the pass energy for the detector was 180 eV for the wide scan and 80 eV for the region scans. For the wide scan a step size of 1 eV and for the region scans a step size of 0.1 eV was applied. All the binding energy values were calibrated using the 1 s photoemission peak for adventitious hydrocarbons at 285 eV.

HR-TEM

TEM measurements were conducted on a double C $_s$ -corrected JEOL ARM 200F with an acceleration voltage of 200 kV. HRTEM images were recorded on a Gatan OneView 4k camera. Electron diffraction patterns were recorded on a Gatan Orius SC200D camera. Images were processed using Gatan Digital Micrograph and ImageJ.

Quantum chemical calculations

All ab initio calculations were performed using the Crystal17 code and its default settings. All optimizations and subsequent frequency calculations were carried out on the DFT-GGA-level with the functional from Perdew-Burke-Ernzerhof (PBE). All-electron LCAO basis sets were applied for P, while effective core potential (ECP) and LCAO valence basis set were used for Sn, and Br. 6 Monkhorst-Pack-type k-points were used for sampling the reciprocal space (a double-density Gilat net of 12 points was used in the calculation of the Fermi energy). The structures were optimized using Grimme's DFT-D3 dispersion correction scheme as implemented in Crystal17 with default parameters. The convergence threshold for the maximum gradient is 0.00045 and for the maximum displacement it is 0.0018. The video files for selected SnBrP vibrations were created using the JMOL software.

Author Contributions

The manuscript was written through contributions of all authors. All authors have given approval to the final version of the manuscript.

Acknowledgements

This research has been supported by the Deutsche Forschungsgemeinschaft (DFG), Grant No. NI1095/8_1, Excellence cluster e-converion (Germany's Excellence Strategy – EXC 2089/1-390776260), and the Diamond light source. F. R., M. P., and A. V. would like to thank the TUM graduate school for continuous support. Open Access funding enabled and organized by Projekt DEAL.

Conflict of Interest

The authors declare no conflict of interest.

Data Availability Statement

The data that support the findings of this study are available from the corresponding author upon reasonable request.

Keywords: One dimensional compound · semiconductor · double helical structure

- [1] M. Bard, I. V. Protopopov, A. D. Mirlin, *Phys. Rev. B* **2019**, *100*, 115153.
- [2] C. Cojan, G. P. Agrawal, C. Flytzanis, *Phys. Rev. B* **1976**, *15*(2), 909–925.
- [3] S. Hasengawa, *J. Phys. Condens. Matter* **2010**, *22*, 084026.
- [4] Z. Fan, H. Razavi, J.-W. Do, A. Moriwaki, O. Ergen, Y.-L. Chueh, P. W. Leu, J. C. Ho, T. Takahashi, L. A. Reichertz, S. Neale, K. Yu, M. Wu, J. W. Ager, A. Javay, *Nat. Mater.* **2009**, *8*, 648–653.
- [5] N. P. Dasgupte, J. Sun, C. Liu, S. Brittman, S. C. Andrews, J. Lim, H. Gao, R. Yan, P. Yang, *Adv. Mater.* **2014**, *26*, 2137–2184.
- [6] S. Liu, Z.-R. Tang, Y. Sun, J. C. Colmenares, Y.-J. Xu, *Chem. Soc. Rev.* **2015**, *44*, 5053–5075.
- [7] X.-C. Dai, S. Hou, M.-H. Huang, Y.-B. Li, T. Li, F.-X. Xiao, *J. Phys. Energy* **2019**, *1*, 022002.
- [8] C. Wang, W. Qui, Y. Zhou, W. Kuang, T. Azhagan, T. Thomas, C. Jiang, S. Liu, M. Yang, *Chem. Eng. J.* **2020**, 122611.
- [9] M. Pavlenko, K. Siuzdak, E. Coy, K. Zaleski, M. Jancelewicz, I. Iatsunskyi, *Int. J. Hydrogen Energy* **2020**, *45*, 26426–26433.
- [10] Z. Sun, H. Zheng, J. Li, P. Du, *Energy Environ. Sci.* **2015**, *8*, 2668–2676.
- [11] G. Kartopu, D. Turkey, C. Ozcan, W. Hadibrata, P. Aurang, S. Yerci, H. E. Unalan, V. Barrioz, Y. Qu, L. Bowen, A. K. Gürlek, P. Maiello, R. Turan, S. J. C. Irvine, *Sol. Energy Mater. Sol. Cells* **2018**, *176*, 100–108.
- [12] P. Karnati, S. Akbar, P. A. Morris, *Sens. Actuators B Chem* **2019**, *295*, 127–143.
- [13] M. M. Arafat, B. Dinan, S. A. Akbar, A. S. M. A. Haseeb, *Sensors* **2012**, *12*, 7205–7258.
- [14] D. Pfister, K. Schäfer, C. Ott, B. Gerke, R. Pöttgen, O. Janka, M. Baumgartner, A. Efimova, A. Hohemann, P. Schmidt, S. Venkatachalam, L. van Wüllen, U. Schürmann, L. Kienle, V. Duppel, E. Parzinger, B. Miller, J. Becker, A. Holleitner, R. Wehrich, T. Nilges, *Adv. Mater.* **2016**, *28*, 9783–9791.
- [15] C. Ott, F. Reiter, M. Baumgartner, M. Pielmeier, A. Vogel, P. Walke, S. Burger, M. Ehrenreich, G. Kieslich, D. Daisenberger, J. Armstrong, U. J. Thakur, P. Kumar, S. Chen, D. Donadio, L. S. Walter, R. T. Weitz, K. Shankar, T. Nilges, *Adv. Funct. Mater.* **2019**, 1900233.
- [16] E. Üzer, P. Kumar, R. Kisslinger, P. Kar, U. K. Thakur, S. Zeng, K. Shankar, T. Nilges, *Appl. Nano Mater.* **2019**, *2*, 6, 3358–3367.
- [17] M. Baumgartner, R. Wehrich, T. Nilges, *Chem. Eur. J.* **2017**, *23*, 6452–6457.
- [18] H. Li, Y. Dai, Y. Ma, M. Li, L. Yu, B. Huang, *J. Mater. Chem. A* **2017**, *5*, 8484.
- [19] K. A. Kovnir, J. V. Zaikina, L. N. Reshetova, A. V. Olenev, E. V. Dikarev, A. V. Shevelkov, *Inorg. Chem.* **2004**, *43*(10), 3230–3236.
- [20] H. Schäfer, *Chemische Transportreaktionen*, in Monographien zu “Angewandte Chemie und Chemie-Ingenieur-Technik,” No. 76, VCH, Weinheim, Germany, 1962, p. 67.
- [21] M. R. P. Pielmeier, A. J. Karttunen, T. Nilges, *J. Phys. Chem. C* **2020**, *124*, 24, 13338–13347.
- [22] D. Pfister, *Reaktivität von Phosphor mit Hauptgruppenmetallhalogeniden*, PhD diss. Technical University Munich, **2017**.
- [23] D. Savytskii, H. Jain, N. Tamura, V. Dierolf, *Sci. Rep.* **2016**, *6*, 36449.
- [24] V. Y. Kolosov, A. R. Thölen, *Acta Mater.* **2000**, *48*, 8, 1829–1840.

Manuscript received: November 15, 2021

Revised manuscript received: December 21, 2021